PAPER

Enhanced anhydrous proton conduction in binary mixtures of 1*H*-imidazole–1*H*-1,2,3-triazole based compounds†

Dipankar Basak,[a] Craig Versek,[b] Jacob A. Harvey,[a] Scott Christensen,[c] Jibben Hillen,‡[a] Scott M. Auerbach,[a] Mark T. Tuominen[b] and D. Venkataraman*[a]

What is the impact of mixing two proton-conducting heterocycles on proton conductivity? Herein we answer this question through our investigations on two linear rod-like compounds 2-(4-(dodecyloxy) phenyl)-1*H*-imidazole (**4**) and 5-(4-(dodecyloxy)phenyl)-1*H*-1,2,3-triazole (**10**). We have found that mixtures of molecules **4** and **10** at certain compositions show enhanced proton conductivity compared to their pure components. We attribute the increased conductivity in these materials to the increased charge density due to facile co-ionization and increased mobility due to the incorporation of long alkyl chains, which prevent crystallization of protogenic groups while maintaining the required hydrogen bonded network. Our results suggest a new strategy for enhancing intrinsic proton conductivity in heterocyclic systems.

1 Introduction

Proton transporting materials that have high intrinsic proton conductivity are highly desirable for fuel cell applications.[1,2] For this purpose high boiling organic heterocycles such as 1*H*-imidazole or 1*H*-1,2,3-triazole have been considered due to their ability to form hydrogen bond networks similar to water.[3–5] Proton conduction in these heterocycles is believed to occur through the Grotthuss mechanism wherein the protons are transported through non-diffusive pathways.[6,7] In general, the magnitude of ion conductivity is described as:

$$\sigma(T) = \sum n_i \mu_i q_i \qquad (1)$$

where $\sigma(T)$ is the conductivity, T is the temperature and q_i, $n_i(T)$ and $\mu_i(T)$ are charge, concentration of the intrinsic charge carriers, and mobility of the charge, respectively.[8] Eqn (1) further indicates that both the charge carrier mobility and the concentration of intrinsic charge carriers will have a profound impact on the overall proton conductivity. Furthermore, for efficient proton transport, it is imperative that the proton-transferring groups organize in such a way that a continuous pathway of

aDepartment of Chemistry, University of Massachusetts Amherst, 710 N. Pleasant Street, Amherst, MA, 01003, USA. E-mail: dv@chem.umass. edu; Fax: +1 4135454490; Tel: +1 4135452028

bDepartment of Physics, University of Massachusetts Amherst, MA, 01003, USA

cDepartment of Polymer Science and Engineering, University of Massachusetts Amherst, MA, 01003, USA

† Electronic supplementary information (ESI) available: DSC, POM, WAXS and NMR spectra. See DOI: 10.1039/c2jm32835f

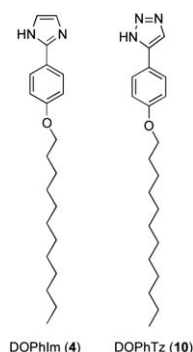‡ Presently a student at Amherst Regional High School, Amherst, MA 01002, USA.

protonic charge carriers exists, with enough flexibility for molecular reorientation of the hydrogen-bonded network.[9–12] This can be achieved *via* immobilization of the heterocycles with flexible linkers (such as long alkyl chains), which satisfies both the requirements.[13,14] At high temperature (above T_g for polymers and above T_m for small molecules), where the mobility of the heterocycles is high it is the number of intrinsic charge carriers that guides the resulting conductivity.[15,16] For *N*-based heterocycles, however, this intrinsic charge carrier concentration is typically low ($\sim$0.1%), resulting from self-dissociation of the protogenic groups.[7,17] Extrinsic doping with strong acids has been carried out to increase this concentration,[6,18,19] but this approach often suffers from potential leaching at high temperatures and a reduction in the proton mobility due to the perturbed hydrogen bonded network upon acid-doping.[7,17] Our initial findings on certain binary mixtures of 1*H*-imidazole and 1*H*-1,2,3-triazole show a significant enhancement in proton conductivity compared to either of the pure compounds.[20] This result suggests that mixing slightly basic 1*H*-imidazole (pK_{a1} = 7.18, pK_{a2} = 14.52)[21] with slightly acidic 1*H*-1,2,3-triazole (pK_{a1} = 1.17, pK_{a2} = 9.26)[5,22] facilitates co-ionization, generating additional charge carriers consisting of imidazolium triazolate. It appears, therefore, that a viable strategy to increase charge carrier density and mobility is to incorporate complementary weak-acid and weak-base into a supramolecular structure.

As model systems we investigate linear rod-like compounds with a long alkyl chain at one end and heterocyclic functionality such as 1*H*-imidazole (**4**) or 1*H*-1,2,3-triazole (**10**) at the other end (Fig. 1). These systems have been designed such that interactions between the long alkyl chains and the protogenic groups will yield a nanoscale organization allowing continuous hydrogen bond pathways, which, coupled with dynamic

20410 | *J. Mater. Chem.*, 2012, **22**, 20410–20417

This journal is © The Royal Society of Chemistry 2012

Fig. 1 Molecular structures of rigid rod-like compounds based on 1*H*-1,2,3-triazole and 1*H*-imidazole.

behaviour, may furnish high proton conductivities. Experiments with several composites of **4** and **10** (complementary mixtures of triazole and imidazole) were performed to understand the impact of effective charge carrier density on the overall proton conductivity. Additionally, by changing the protogenic group from 1*H*-1,2,3-triazole to 1*H*-imidazole in these small molecule systems, we are able to investigate the impact of each heterocycle in a nearly identical structural environment. This systematic study investigating the role of charge carrier density in a system with nanoscale domains is an important step towards setting the design criteria for co-polymers with complimentary heterocycles for next generation polymer electrolyte membranes.

2   Experimental section

2.1   Materials and characterization

All ^{1}H and ^{13}C NMR spectra were recorded on a Bruker DPX 400 MHz spectrometer. Chemical shift (δ) and coupling constant (J) are reported in parts per million and Hertz, respectively. The abbreviations for splitting patterns are s, singlet; bs, broad singlet; d, doublet; t, triplet; q, quartet; dd, doublet of doublets, and m, multiplet. TGA was carried out using a TA Instruments TGA 2950 thermogravimetric analyzer with a heating rate of 10 °C min^{-1} from room temperature to 600 °C under nitrogen. Differential scanning calorimetry (DSC) was performed on a Mettler–Toledo model DSC 822^c differential scanning calorimeter, where temperature and enthalpy were calibrated with In (430 K, 3.3 J mol^{-1}) and Zn (692.7 K, 12 J mol^{-1}) standard samples using sealed Al sample pans. Cooling and heating profiles were recorded and analyzed using the Mettler–Toledo STAR^c software system. Optical microscopy was performed on a Zeiss Axiotech Vario reflected light microscope under crossed polarizers, equipped with an Instec HCS62N hot stage. X-Ray scattering was done using an in-house setup from Molecular Metrology Inc. (presently sold as Rigaku S-Max3000). It uses a 30 W microsource (Bede) with a 30×30 μm^2 spot size matched to a Maxflux® optical system (Osmic) leading to a low-divergence beam of monochromatic CuK$_\alpha$ radiation (wavelength λ = 0.1542 nm). After passing beam defining and guard pinholes, the beam of about 0.4 mm diameter enters the sample chamber. Samples were placed within a hot stage connected to an Omega CN76000 temperature controller. WAXS is performed using an image plate (maximum resolution 50 μm) positioned in the

sample chamber at a distance of 139 mm. The whole system is evacuated. The actual scattering angles are calibrated using the accurately known reflections from silver behenate and tricosane. Mass spectroscopic methods were performed by the Mass Spectrometry Center at the University of Illinois, Urbana-Champaign. Impedance data were obtained using a Solartron 1260 frequency response analyzer in the range of 0.1 Hz to 10 MHz with a sinusoidal excitation voltage of 0.1 V root-mean-square amplitude. Vacuum dried samples were placed into a cavity (L = 0.029 cm long by A = 0.079 cm^2 cross-sectional area) of a PTFE tape spacer between two gold-coated stainless steel electrodes. The sample's resistance to proton transport, R, was estimated by fitting a constant value to the plateau of impedance magnitude, which occurred within this frequency range. Conductivity was computed as $\sigma = L/(RA)$. Measurements were conducted in an ESPEC SH-241 temperature control chamber between 40 °C and 150 °C with a sweep rate of 0.25 °C min^{-1}.

All reactions were carried out in oven-dried glassware (160 °C). The chemicals were purchased from major chemical suppliers (Acros, Sigma-Aldrich, Alfa-Aesar and TCI America) and were used without further purification unless otherwise noted. Triethylamine and dichloromethane were redistilled over anhydrous calcium hydride and stored over 4 Å molecular sieves under argon. Flash chromatography was performed using silica gel from Sorbent Technologies (Standard Grade, 60 Å, 230–400 mesh). Analytical thin layer chromatography was performed on a pre-coated silica gel glass plate with visualization under UV light. *N*-Bromosuccinimide (NBS) was recrystallized from water. 4-(Dodecyloxy)benzaldehyde (**2**),[23] 1-(dodecyloxy)-4-ethynylbenzene (**8**),[24] and azidomethyl pivalate[25] were synthesized according to the reported literature procedures, respectively.

2-(4-(Dodecyloxy)phenyl-4,5-dihydro-1*H*-imidazole (3). Compound **3** was synthesized from compound **2** according to the procedure reported in the literature.[26] Pale yellow solid. Yield: 69%. ^{1}H NMR (CDCl$_3$, 400 MHz) δ 7.74 (d, J = 9.2 Hz, 2H), 6.88 (d, J = 9.2 Hz, 2H), 4.86 (bs, 1H), 3.96 (t, J = 6.8 Hz, 2H), 3.76 (s, 4H), 1.78 (quintet, J = 6.8 Hz, 2H), 1.46–1.26 (m, 18H), 0.87 (t, J = 6.8 Hz, 3H); ^{13}C NMR (CDCl$_3$, 101 MHz) δ 164.4, 161.1, 128.5, 122.7, 114.2, 68.1, 31.9, 29.7, 29.66, 29.63, 29.60, 29.57, 29.39, 29.35, 29.18, 26.0, 22.7, 14.1; HRMS (ESI) *m/z* calcd for C$_{21}$H$_{35}$N$_2$O [M + H]$^+$: 331.2749; found: 331.2746.

2-(4-(Dodecyloxy)phenyl)-1*H*-imidazole (4). Compound **3** was converted to compound **4** according to the procedure reported in the literature.[26] Pale yellow solid. Yield: 78%. ^{1}H NMR (CDCl$_3$, 400 MHz) ^{1}H NMR (CDCl$_3$, 400 MHz) δ 7.75 (d, J = 8.8 Hz, 2H), 7.11 (s, 2H), 6.96 (d, J = 9.2 Hz, 2H), 3.97 (t, J = 6.8 Hz, 2H), 1.79 (quintet, J = 6.8 Hz, 2H), 1.47–1.26 (m, 18H), 0.88 (t, J = 6.8 Hz, 3H); ^{13}C NMR (CDCl$_3$, 101 MHz) δ 159.7, 146.9, 126.6, 122.9, 114.9, 68.1, 31.9, 29.67, 29.65, 29.61, 29.59, 26.41, 29.36, 29.2, 26.0, 22.7, 14.1; HRMS (ESI) *m/z* calcd for C$_{21}$H$_{33}$N$_2$O [M + H]$^+$: 329.2593; found: 329.2587.

(5-(4-(Dodecyl)phenyl)-1*H*-1,2,3-triazol-1-yl)methyl pivalate (9). In a single-necked round bottom flask a mixture of **8** (0.86 g, 3.0 mmol) and CuI (0.29 g, 1.5 mmol) were taken together under argon. To the mixture a solution of *N*,*N*-diisopropylethylamine (1.60 mL, 9.0 mmol), 0.72 g (4.50 mmol) of azidomethyl pivalate

in 40 mL of deoxygenated THF were added and stirred at 50 °C for 12 h. The reaction mixture was cooled down to room temperature after 12 h and 60 mL of water was added. The organic layer was extracted with dichloromethane (2 × 60 mL), washed with water (2 × 50 mL), brine (2 × 50 mL), dried over anhydrous Na_2SO_4 and concentrated under reduced pressure. The crude product was purified by column chromatography (4 : 0.5 hexane–ethyl acetate) to afford 1.2 g of **9** (90%) as a white solid.

^{1}H NMR (CDCl$_3$, 400 MHz) ^{1}H NMR (CDCl$_3$, 400 MHz) δ 7.93 (s, 1H), 7.76 (d, J = 8.8 Hz, 2H), 6.95 (d, J = 8.8 Hz, 2H), 6.26 (s, 2H), 3.98 (t, J = 6.6 Hz, 2H), 1.79 (quintet, J = 6.8 Hz, 2H), 1.47–1.26 (m, 18H), 1.19 (s, 9H), 0.88 (t, J = 6.8 Hz, 3H); ^{13}C NMR (CDCl$_3$, 101 MHz) δ 178.0, 159.4, 148.3, 127.1, 122.5, 120.0, 114.9, 69.7, 68.1, 38.8, 31.9, 29.67, 29.64, 29.60, 29.59, 26.41, 29.36, 29.25, 26.8, 26.0, 22.7, 14.1; HRMS (ESI) m/z calcd for $C_{26}H_{42}N_3O_3$ [M + H]$^+$: 444.3226; found: 444.3233.

5-(4-(Dodecyloxy)phenyl)-1H-1,2,3-triazole (10). In a single-necked round bottom flask **9** (1.1 g, 2.48 mmol) was dissolved in 30 mL of 0.5 M NaOH/THF (1 : 1 v/v mixture) and the mixture was heated at 50 °C for 12 h. The reaction mixture was cooled down to room temperature, 20 mL water was added to it and pH was adjusted to 7.0 by dropwise addition of 1 M HCl. The mixture was filtered off, washed with water and dried under vacuum. The product was further purified by eluting through a small pad silica column (3% MeOH/CHCl$_3$) to afford **10** as a white solid (quantitative yield). ^{1}H NMR (DMSO-d$_6$, 400 MHz) δ 14.95 (bs, 1H), 8.23 (s, 1H), 7.79 (d, J = 8.4 Hz, 2H), 7.03 (d, J = 8.4 Hz, 2H), 4.02 (t, J = 6.4 Hz, 2H), 1.794 (quintet, J = 6.4 Hz, 2H), 1.44–1.27 (m, 18H), 0.88 (t, J = 6.8 Hz, 3H); ^{13}C NMR (DMSO-d$_6$, 101 MHz) δ 159.1, 127.4, 115.3, 67.9, 31.8, 29.5, 29.49, 29.46, 29.2, 29.19, 29.12, 25.9, 22.6, 14.1; HRMS (ESI) m/z calcd for $C_{20}H_{32}N_3O$ [M + H]$^+$: 330.2545; found: 330.2549.

3 Results and discussions

3.1 Synthesis

2-(4-(Dodecyloxy)phenyl)-1H-imidazole (**4**) was synthesized from 4-hydroxybenzaldehyde (**1**) using the well-established literature procedure (Scheme 1).[26] **1** was alkylated to **2** via Williamson's ether synthesis; the latter was then converted to imidazoline compound (**3**) by reacting with ethylenediamine.[27] Swern oxidation[28] of **3** furnished the desired imidazole derivative **4** as a pale yellow solid in 78% yield.

5-(4-(Dodecyloxy)phenyl)-1H-1,2,3-triazole (**10**) was obtained from 4-iodophenol in five steps (Scheme 2). 1-(Dodecyloxy)-4-ethynylbenzene (**8**) was obtained using Sonogashira coupling[29] between compound **6** and TMS-acetylene using Cu(ı)/Pd(0) in the presence of triethylamine as base, followed by TMS-cleavage

Scheme 1 Synthetic route for DOPhIm (**4**).
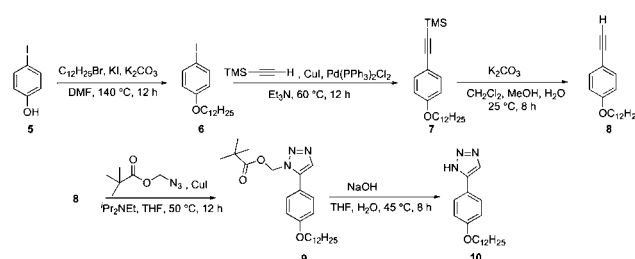
Scheme 2 Synthetic route for DOPhTz (**10**).

under mild basic conditions. The alkyne group was then converted to pivolyloxymethyl protected 1,2,3-triazole moiety (**9**) using azide-alkyne-Huisgen dipolar cycloaddition reaction.[30,31] The deprotection of the pivolyloxymethyl group in the presence of 0.5 M NaOH furnished compound **10** as a white solid.[25]

3.2 Thermal analysis

Thermal stability of **4**, **10** and their mixtures was tested by thermogravimetric analysis (TGA) with a heating rate of 10 °C min^{-1} under a nitrogen atmosphere. Solid samples were kept *in vacuo* for 12 h before recording TGA data. DOPhIm (**4**) and DOPhTz (**10**) were mixed at different compositions and heated to 140 °C for 1 h and then cooled (5 °C min^{-1}) back slowly to room temperature to ensure intimate mixing. TGA plots of DOPhIm (**4**), DOPhTz (**10**) and their mixture of different compositions showed minimal weight loss before 230 °C, indicating the thermal stability of the components at least up to 230 °C (Fig. 2). A continuous weight loss was observed after 250 °C, presumably due to decomposition of the hydrocarbon.

Thermal properties of DOPhTz (**10**) and DOPhIm (**4**) and their different compositions were studied by differential scanning calorimetry (DSC). DSC traces were recorded between −30 °C and 200 °C with a heating and cooling rate of 10 °C min^{-1} and 5 °C min^{-1}, respectively. The composites were heated up to 200 °C to remove any thermal history (first heating), followed by slow cooling (first cooling cycle) and subsequent heating (second heating cycle) (Fig. 3). Upon second heating DOPhTz (**10**) shows a single endotherm at 138.7 °C, corresponding to the crystal (K) to isotropic (I) transition. The transition is fully reversible as one exotherm corresponding to the crystallization arrives at 130.7 °C
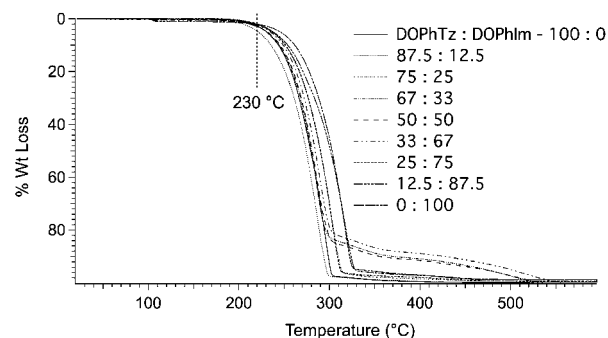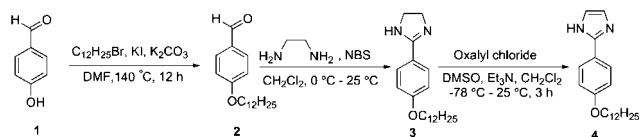

Fig. 2 Thermogravimetric analysis (TGA) of DOPhIm(**4**)–DOPhTz(**10**) composites (heating rate 10 °C min^{-1}), the composites show minimal weight loss at least up to 230 °C.
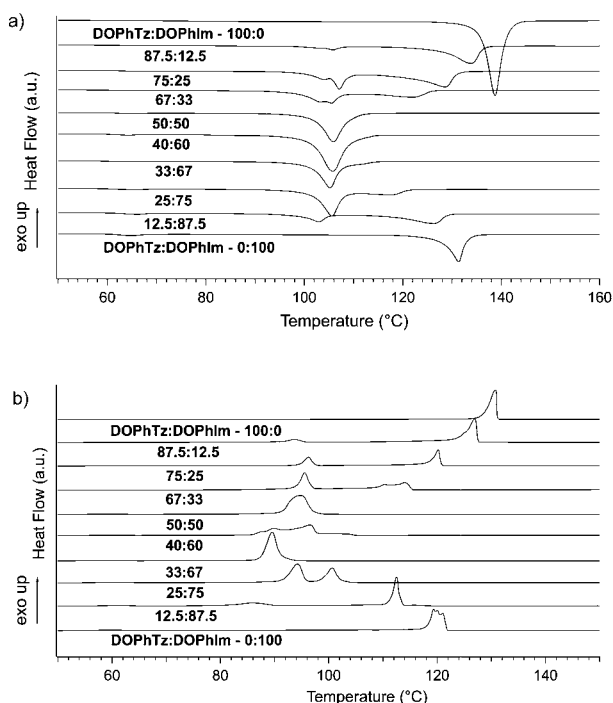
Fig. 3 DSC profiles for different DOPhIm(**4**)–DOPhTz(**10**) composites. (a) 2nd heating cycle (10 °C min⁻¹) and (b) 1st cooling cycle (5 °C min⁻¹). All the transitions were completely reversible in the heating and cooling cycles.

during the cooling cycle. Polarized optical micrographs (POM) of DOPhTz (**10**) above 140 °C show no birefringence indicating an isotropic phase, while cooling the sample below 130 °C results in birefringence, indicating crystallization (see Fig. S2 in the ESI†). Upon heating, DOPhIm (**4**) shows a broad endotherm at 131.3 °C, corresponding to the crystal (K) to isotropic (I) phase transition, which was further supported by POM (Fig. S1 in the ESI†). Similar to DOPhTz (**10**), an exotherm arises at 119.3 °C, indicating a fully reversible phase transition. Most of the DOPhTz(**10**)–DOPhIm(**4**) composites exhibit two endotherms during heating, corresponding to two-phase transitions (K₁ to K₂ and K₂ to I), which are fully reversible during the subsequent cooling cycles. However, the composites DOPhTz(**10**)–DOPhIm(**4**) = 40/60, 50/50 and 33.3/66.7 exhibit one endotherm during the heating cycle, corresponding to only one K to I transition. Details of transition temperatures and associated enthalpy changes are summarized in Table T1 of the ESI.†

The phase diagram of DOPhIm(**4**)–DOPhTz(**10**) composites is shown in Fig. 4. All the compositions are solid at room temperature and the melting points (T_m) of the composites are lower than the T_m of either DOPhTz (**10**) or DOPhIm (**4**). As the mole fraction of DOPhIm (**4**) increases, the T_m of the composites decreases until they form an equimolar mixture (50/50 DOPhIm(**4**)–DOPhTz(**10**)). Furthermore, two other composites DOPhIm(**4**)–DOPhTz(**10**) = 60/40 and 66.7/33.3 show similar T_m, indicating a range of eutectic compositions. When the mole fraction of DOPhIm (**4**) increases further, the T_m of the composites again increases. The second melting peaks remain invariant with composition, located close to the T_m of the eutectic compositions.
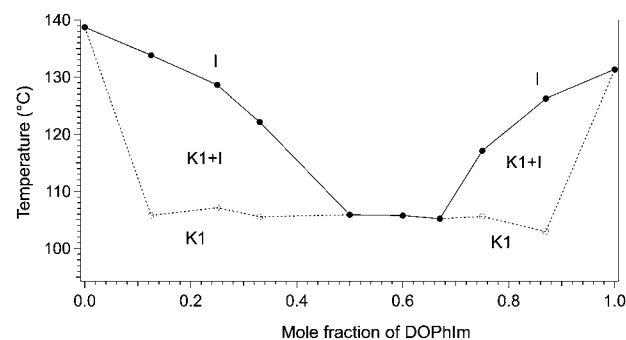

Fig. 4 Phase diagram for different DOPhIm(**4**)–DOPhTz(**10**) composites. The data points were extracted from the second heating cycle in DSC. Except some intermediate compositions, most of the composites show two distinct phases: the crystalline state is labeled as K₁, the isotropic state is labeled as I and the intermediate state is labeled as K₁ + I.

3.3 Anhydrous proton conduction

The temperature dependence of proton conductivities for various DOPhIm(**4**)–DOPhTz(**10**) composites were studied by impedance spectroscopy and are shown in Fig. 5. All samples were heated to 140 °C, the highest temperature recorded, and conductivities were measured during slow cooling of the samples at the rate of 0.25 °C min⁻¹. The anhydrous proton conductivity of DOPhIm (**4**) was 1.3×10^{-4} S cm⁻¹ at 140 °C, at least three orders of magnitude higher than that of DOPhTz (**10**) (7.4×10^{-7} S cm⁻¹) at the same temperature. A sharp slope change in $\log(\sigma)$ vs. $1/T$ plot was observed for both DOPhIm (**4**) (at 123 °C) and DOPhTz (**10**) (at 134 °C), corresponding to the isotropic to crystalline phase transitions, correlating well with the transitions observed in DSC. This drastic drop in the conductivity curve further indicates that dynamic hydrogen bonding of a locally liquid-like state is critical for anhydrous proton conduction, in agreement with our previous report on discotic liquid crystalline proton conductors.

Fig. 6 shows the composition dependence of isothermal proton conductivities of different DOPhIm(**4**)–DOPhTz(**10**) composites. Neat DOPhTz (**10**) shows the lowest conductivity (*e.g.* 7.4×10^{-7} S cm⁻¹ at 140 °C) of any composition investigated, and increasing the mole fraction of DOPhIm (**4**) increases the proton conductivity until it reaches a local maximum at
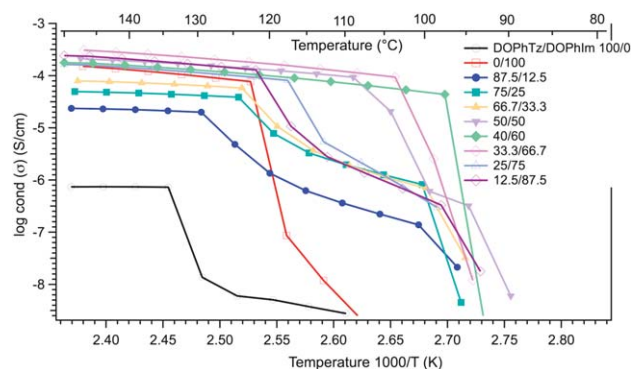

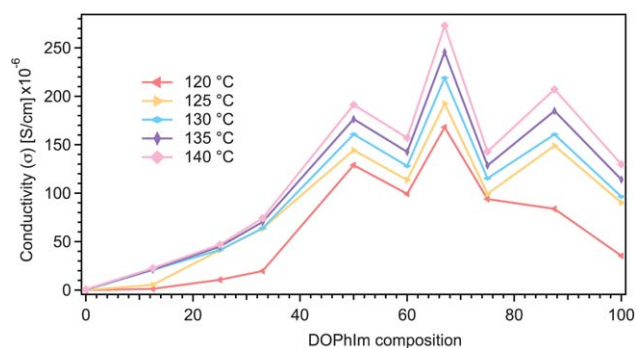**Fig. 5** Anhydrous proton conductivities of different DOPhIm(**4**)–DOPhTz(**10**) composites.

This journal is © The Royal Society of Chemistry 2012

J. Mater. Chem., 2012, **22**, 20410–20417 | **20413**

Fig. 6 Isothermal anhydrous proton conductivities of different DOPhIm(**4**)–DOPhTz(**10**) composites as a function of DOPhIm (**4**) mole fraction.

DOPhTz(**10**)–DOPhIm(**4**) = 50/50. At this 50/50 composition, a conductivity at 140 °C of 1.9×10^{-4} S cm^{-1} is observed, prior to a drop at DOPhTz(**10**)–DOPhIm(**4**) = 40/60. A similar trend is followed in the DOPhIm(**4**) rich range, wherein an increase in conductivity is observed at DOPhTz(**10**)–DOPhIm(**4**) = 12.5/87.5 (2.0×10^{-4} S cm^{-1} at 140 °C) prior to a decrease at DOPhTz(**10**)–DOPhIm(**4**) = 25/75. Among all the compositions, the highest conductivity is observed at DOPhTz(**10**)–DOPhIm(**4**) = 33.3/66.7, which is in the range of eutectic compositions. At 140 °C, the peak conductivity is 2.7×10^{-4} S cm^{-1}, which is three orders of magnitude higher than the conductivity of neat DOPhTz (**10**) and slightly higher than neat DOPhIm (**4**) (1.3×10^{-4} S cm^{-1}) at the same temperature.

3.4 Powder X-ray scattering

Structures of neat DOPhTz (**10**), DOPhIm (**4**) and their equimolar composite DOPhTz(**10**)–DOPhIm(**4**) (50/50) were characterized using small- and wide-angle X-ray scattering. A distinct scattering peak is observed for neat DOPhTz (**10**) in SAXS, while neat DOPhIm (**4**) remains featureless in this range, necessitating wide-angle scattering for this sample. Further investigation of DOPhTz (**10**) was performed using variable temperature SAXS, with Fig. 7b showing results recorded upon slow cooling from 160 °C to 25 °C. Upon heating to 160 °C, beyond the phase transition temperature, a diffuse broad peak arises at $q = 1.61$ nm^{-1}, indicating a poorly ordered, liquid-like material with a characteristic length scale of 3.91 nm. The lack of birefringence observed in POM at this temperature further indicates poorly defined organization. Upon cooling to 80 °C, the primary peak shifts to $q = 1.49$ nm^{-1}, corresponding to a characteristic spacing of 4.22 nm, which was further sharpened upon cooling to 25 °C. Although the structure cannot be determined unambiguously from these data, it is notable that the fully extended length of DOPhTz (**10**) as calculated by DFT optimized at the B3LYP/6-311 G(d,p) level is 2.3 nm (Fig. 7a). The estimated thickness of 'head-to-head' stacking of the triazole-functionalized dodecyl alkyl chains will therefore be 4.6 nm, very close to the observed spacing of $d = 4.22$ nm. This analysis suggests the presence of bilayer domains in **10** (Fig. 7c). The increase in length scale observed (from $d = 3.91$ nm to $d = 4.22$ nm) upon cooling likely reflects the increased mobility of the alkyl chains at high

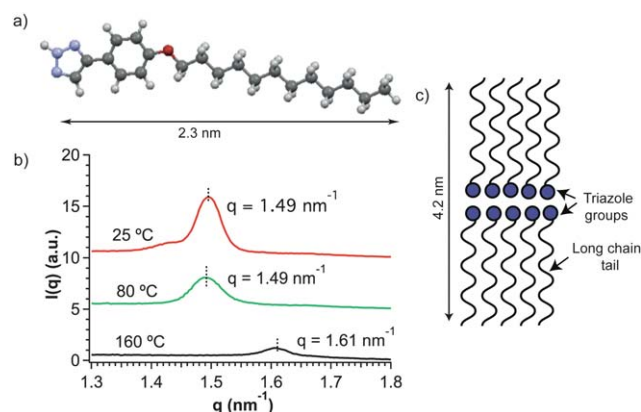**Fig. 7** (a) DFT optimized at the B3LYP/6-31 G level of DOPhTz (**10**) estimating the molecular length of ∼2.3 nm; (b) SAXS profile of DOPhTz (**10**) at different temperatures: samples were initially heated to 160 °C and subsequently cooled down to 80 °C and 25 °C. $I(q)$ values have been shifted vertically for clarity; (c) an illustration of the proposed structure of DOPhTz (**10**), which self-assembles into a head-to-head bilayer type packing.
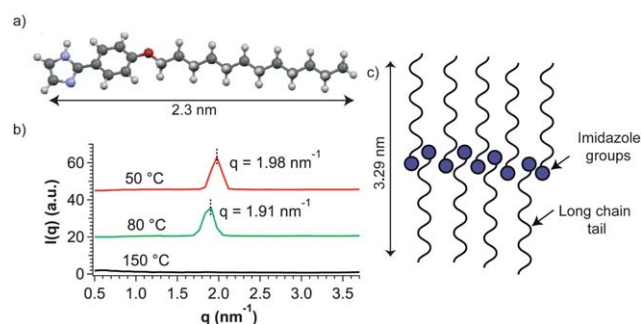

Fig. 8 (a) DFT optimized at the B3LYP/6-31 G level of DOPhIm (**4**) estimating the molecular length of ∼2.3 nm; (b) WAXS profile of DOPhIm (**4**) at different temperatures: samples were initially heated to 150 °C and subsequently cooled down to 80 °C and 50 °C. $I(q)$ values have been shifted vertically for clarity; (c) an illustration of the proposed structure of DOPhIm (**4**), which self-assembles into an interdigitated bilayer type packing.

temperature, causing them to become less extended, decreasing layer thickness and ordering in the system.

Fig. 8b shows wide-angle X-ray scattering (WAXS) of DOPhIm (**4**) recorded at variable temperatures. For comparison purposes, only the primary peak is shown in Fig. 8 (full WAXS spectrum is shown in the ESI Fig. S3†). Upon heating to 150 °C (beyond the phase transition temperature) no scattering peak was observed, indicating an isotropic phase, consistent with the DSC observation. Upon subsequent cooling to 80 °C, a well-resolved scattering peak appeared at $q = 1.91$ nm^{-1}, indicating the emergence of a characteristic length scale of 3.29 nm. This value is much lower than that for head-to-head packing of fully stretched dodecyl chains with imidazole functionality (∼4.6 nm – Fig. 8a), and as such suggests an interdigitated structure obtained through side-to-side hydrogen bonding of adjacent imidazole groups (Fig. 8c). The single crystal X-ray structure of 2-[4-(decyloxy)-phenyl]-1H-imidazole reported in the literature[26] exhibits extended chains of hydrogen bonding as well as
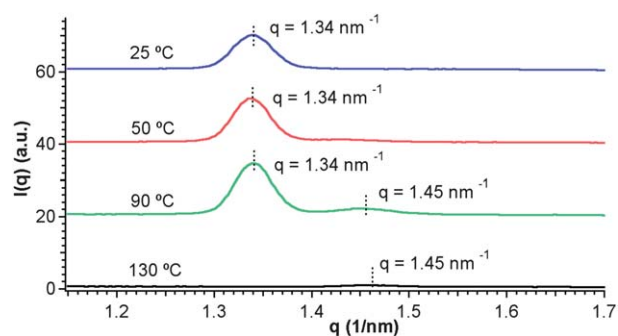
20414 | *J. Mater. Chem.*, 2012, **22**, 20410–20417

This journal is © The Royal Society of Chemistry 2012

Fig. 9 SAXS profile of DOPhTz(**10**)–DOPhIm(**4**) composite 50/50 at different temperatures: samples were initially heated to 130 °C and subsequently cooled down to 25 °C. $I(q)$ values have been shifted vertically for clarity.

interdigitation of the imidazole rings, further supporting our speculation of an interdigitated bilayer type packing for DOPhIm (**4**) from variable temperature WAXS observations.

The structure of DOPhIm(**4**)–DOPhTz(**10**) composite (50/50) was further investigated using small angle X-ray scattering at various temperatures (Fig. 9). Upon heating to 130 °C, a diffuse broad peak arises at $q = 1.45$ nm^{-1}, indicating a poorly ordered, liquid-like material with a characteristic length scale of 4.34 nm. Upon cooling to 90 °C, a broad primary peak falls at $q = 1.34$ nm^{-1} ($d = 4.69$ nm) and a second, diffuse peak centers on the original peak position at 130 °C ($q = 1.45$ nm^{-1}). Based on the persistence of the secondary peak, we speculate that a portion of the composite does not crystallize completely at this temperature (DSC cooling curve of 50/50 composite also shows a broad temperature regime of crystallization) and the peak location and breadth are due to the liquid-like nature of the aliphatic chains. Upon further cooling to 50 °C, a single peak persists at $q = 1.34$ nm^{-1}, suggesting complete crystallization. The characteristic length scale of 4.69 nm further indicates that the composite maintains a bilayer type 'head-to-head' stacking as observed in the packing of DOPhTz (**10**) component. It is also notable that the characteristic spacing ($d = 4.69$ nm) of the composite is higher than either DOPhIm (**4**) ($d = 3.29$ nm) or DOPhTz (**10**) ($d = 4.2$ nm), suggesting swelling of the head-to-head DOPhTz (**10**) domains *via* incorporation of interdigitating DOPhIm (**4**) (*vide infra*).

Combining these X-ray scattering results with our conductivity measurements provides insight into the nature of proton transport in both imidazole-(DOPhIm (**4**)) and triazole-containing (DOPhTz (**10**)) supramolecular architectures. It is known in the literature that in the crystal state, 1,2,3-triazole can exist in equal proportions of two tautomeric forms – 1*H*-1,2,3-triazole and 2*H*-1,2,3-triazole (in the gas phase 2*H*-1,2,3-triazole is the predominant form while 1*H*-1,2,3-triazole becomes increasingly more stable with an increase in the polarity of the medium).[32] Based on these and further studies elucidating the possible proton transfer mechanisms in 1,2,3-triazole, we envision that DOPhTz (**10**) can exhibit two types of hydrogen bonding – extended bonds in the same layer using two side N atoms of the triazole ring (so-called *imidazole-like* pathway[33] – Fig. 10b), and localized bonds using the middle and one of the side N atoms (so-called *pyrazole like* pathway[33] – Fig. 10a). The head-to-head
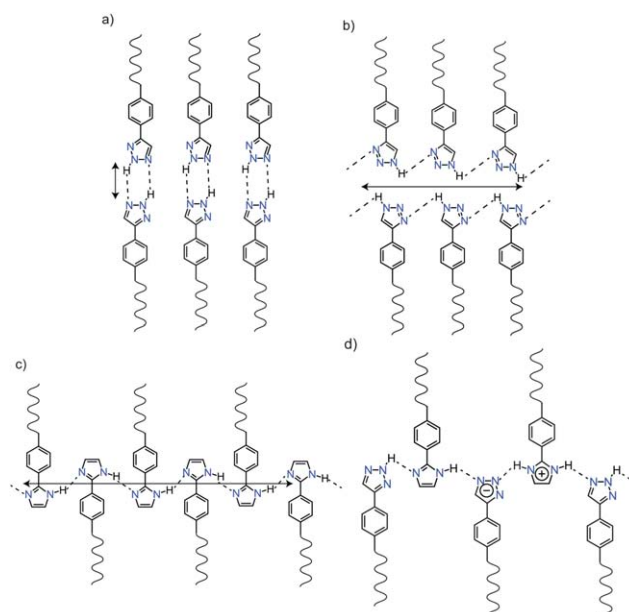

Fig. 10 Illustration of hypothetical proton conduction pathways for DOPhTz (**10**) (a) and (b); (c) DOPhIm (**4**) and (d) equimolar composite of DOPhIm(**4**)–DOPhTz(**10**) – 50/50. While extended hydrogen bonding exists in DOPhIm (**4**) and in the composite, the predominant presence of hydrogen bond clusters results in poor performance for DOPhTz (**4**).

packing observed in DOPhTz (**10**) presumably supports the predominant existence of pyrazole-like pathways, resulting in hydrogen-bonded clusters with low charge mobility, yielding a low overall conductivity. Conversely, as X-ray scattering data support, DOPhIm (**4**) forms interdigitated structures through side-to-side hydrogen bonding between adjacent imidazole rings (Fig. 10c).[26] Therefore, while DOPhTz (**10**) forms local hydrogen bonds, DOPhIm (**4**) forms extended one-dimensional hydrogen bonded networks, increasing protonic charge mobility and favouring long-range Grotthuss-type proton transport. Although the exact mechanism of proton transfer is still unclear and requires further attention, this result confirms that a change in the protogenic group from 1*H*-imidazole to 1*H*-1,2,3-triazole has a significant influence on charge mobility in supramolecular systems. While the nanoscale organization of protogenic groups has previously proven beneficial to proton conductivity, care must be taken to achieve a packing of heterocycles, which yields an extended hydrogen-bonded network *versus* locally hydrogen-bonded clusters.

Based solely on this argument of extended *vs.* local hydrogen bonding, DOPhIm (**4**), with the most imidazole-like hydrogen bonds, would have the highest conductivity of any composition measured. This is clearly not the case, however, as incorporating up to 50 percent DOPhTz (**10**) increases measured conductivity while presumably decreasing the occurrence of these favorable pathways. X-ray data for the equimolar mixture of DOPhTz(**10**)–DOPhIm(**4**) does suggest that DOPhIm (**4**) interpenetrates into the hydrogen bonded network of DOPhTz (**10**) and facilitates the formation of imidazole-like bonding in the composite (Fig. 10d), yet this alone cannot account for the enhanced conductivity of the composite mixtures. In order to understand the effect of complementary weak-acid–base
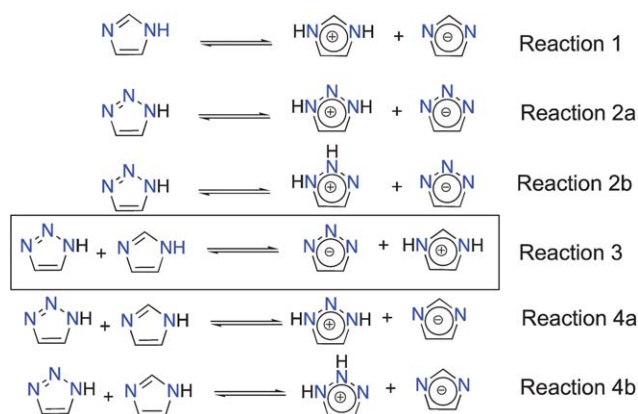
This journal is © The Royal Society of Chemistry 2012

J. Mater. Chem., 2012, **22**, 20410–20417 | 20415

Fig. 11 Auto-ionization and co-ionization of imidazole, triazole and imidazole–triazole composites.

interactions between 1H-1,2,3-triazole and 1H-imidazole, we initiated a computational study.

3.5 Computational studies

To determine the trend in charge carrier density, a thermochemistry analysis was performed using the Gaussian09 software package.[34] Structures of neutral, protonated, and deprotonated imidazole and 1,2,3-triazole were optimized using a 6-311G(d,p) basis set and the B3LYP hybrid density functional. Triazole may be protonated at adjacent or opposite positions, producing a total of six distinct auto- and cross-ionization reactions, listed below (Fig. 11). The standard Gibbs free energy for each isolated reactant under fictitious, ideal-gas conditions at STP was determined from a subsequent frequency calculation using Gaussian09. Standard reaction ΔG values for the six distinct reactions below were then computed and used to calculate each reaction K_{eq}, which is, in principle, proportional to the charge carrier density notwithstanding the environmental effects of solid-state packing. Because the solids synthesized and studied herein are likely to be low-dielectric materials, we do not expect solvation effects to control the actual ionization thermochemistry, and thus the gas-phase trends should remain qualitatively
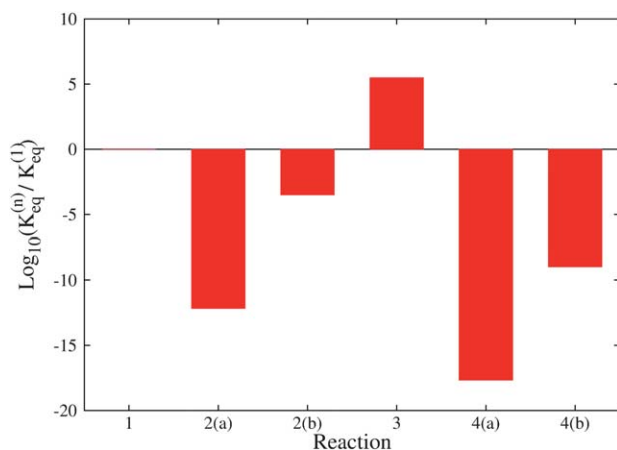
correct. These K_{eq} values were referenced to the result for imidazole auto-ionization (Reaction 1 below) and are plotted on a logarithmic scale i.e., K_{eq} values are shown as $\log_{10}(K_{eq}^{(n)}/K_{eq}^{(1)})$ where $K_{eq}^{(n)}$ is the K_{eq} value for the nth reaction.

The standardized reaction K_{eq} values are shown in Fig. 12. We note that the auto-ionization of imidazole is predicted to be more likely than that of triazole (Reactions 2a/2b). This is consistent with the experimental result that the conductivity of DOPhIm is greater than that of DOPhTz. In addition, we observe the particularly interesting result that K_{eq} for Reaction 3, in which triazole protonates imidazole, is the largest value computed herein. This suggests that the charge carrier density is expected to be greatest in an imidazole–triazole mixture, which may lead to an increase in conductivity, all other things being equal. Although Reactions 4a and 4b also pertain to the mixture, they are rather unlikely because imidazole acts as the acid, which in contrast to the pK_a values of imidazole and triazole as described above. These results suggest that the charge carrier density is expected to be greatest in mixtures of these functional groups, which is consistent with the experimentally obtained enhanced conductivity values.

4 Conclusion

We have synthesized two linear rod-like compounds based on 1H-imidazole and 1H-1,2,3-triazole proton transferring functionalities and investigated their anhydrous proton conductivities. The 1H-1,2,3-triazole-based compound DOPhTz (**10**) exhibited anhydrous proton conductivity at least three orders of magnitude lower than the conductivity of a 1H-imidazole-based compound DOPhIm(**4**) at the same temperature. The thermal behavior of these two compounds was found to be nearly identical, however, X-ray data support head-to-head bilayer type packing for DOPhTz (**10**) while an interdigitated structure through sideways hydrogen bonding is observed for DOPhIm (**4**). The enhanced conductivity of DOPhIm (**4**) is attributed to the formation of extended hydrogen bonded networks through an imidazole-like arrangement, while DOPhTz (**10**) primarily exists in pyrazole-like locally hydrogen bonded clusters. Mixing of the two materials in complementary acid–base composites demonstrates a potential increase in charge carrier density associated with co-ionization of 1H-imidazole and 1H-1,2,3-triazole, with maximum conductivity observed at a DOPhTz(**10**)–DOPhIm(**4**) ratio of 1/2. We conclude that to increase charge carrier density and mobility in anhydrous supramolecular systems, it is favourable to select complementary protogenic groups, which self-assemble into global hydrogen bonded networks. As a result, we are currently investigating new copolymers containing complementary acid–base pairs, which we hope to publish in due course.

Fig. 12 Standardized K_{eq} for auto-ionization and co-ionization reactions. Reaction 3 has the largest K_{eq} value, indicating facile co-ionization of imidazole (weak base) and triazole (weak acid).

20416 | *J. Mater. Chem.*, 2012, **22**, 20410–20417

This journal is © The Royal Society of Chemistry 2012

Notes and references

1 K. D. Kreuer, *Chem. Mater.*, 1996, **8**, 610–641.
2 L. Carrette, K. A. Friedrich and U. Stimming, *Fuel Cells*, 2001, **1**, 5–39.
3 M. F. H. Schuster, W. H. Meyer, M. Schuster and K. D. Kreuer, *Chem. Mater.*, 2004, **16**, 329–337.
4 H. G. Herz, K. D. Kreuer, J. Maier, G. Scharfenberger, M. F. H. Schuster and W. H. Meyer, *Electrochim. Acta*, 2003, **48**, 2165–2171.
5 Z. Zhou, S. W. Li, Y. L. Zhang, M. L. Liu and W. Li, *J. Am. Chem. Soc.*, 2005, **127**, 10824–10825.
6 M. E. Schuster and W. H. Meyer, *Annu. Rev. Mater. Res.*, 2003, **33**, 233–261.
7 K. D. Kreuer, S. J. Paddison, E. Spohr and M. Schuster, *Chem. Rev.*, 2004, **104**, 4637–4678.
8 A. R. West, *Basic Solid State Chemistry*, Wiley Chichester, West Sussex, UK, 1988.
9 D. Basak, S. Christensen, S. K. Surampudi, C. Versek, D. T. Toscano, M. T. Tuominen, R. C. Hayward and D. Venkataraman, *Chem. Commun.*, 2011, **47**, 5566–5568.
10 C.-F. Chow, V. A. L. Roy, Z. Ye, M. H. W. Lam, C. S. Lee and K. C. Lau, *J. Mater. Chem.*, 2010, **20**, 6245–6249.
11 K. D. Kreuer, *Solid State Ionics*, 1997, **94**, 55–62.
12 J. A. Harvey, D. Basak, D. Venkataraman and S. M. Auerbach, *Mol. Phys.*, 2012, **110**, 957–966.
13 M. Schuster, W. H. Meyer, G. Wegner, H. G. Herz, M. Ise, K. D. Kreuer and J. Maier, *Solid State Ionics*, 2001, **145**, 85–92.
14 J. C. Persson and P. Jannasch, *Chem. Mater.*, 2003, **15**, 3044–3045.
15 R. C. Woudenberg, O. Yavuzeetin, M. T. Tuorninen and E. B. Coughlin, *Solid State Ionics*, 2007, **178**, 1135–1141.
16 C. A. Alabi, Z. Chen, Y. S. Yan and M. E. Davis, *Chem. Mater.*, 2009, **21**, 4645–4652.
17 M. Schuster, T. Rager, A. Noda, K. D. Kreuer and J. Maier, *Fuel Cells*, 2005, **5**, 355–365.
18 S. Granados-Focil, R. C. Woudenberg, O. Yavuzcetin, M. T. Tuominen and E. B. Coughlin, *Macromolecules*, 2007, **40**, 8708–8713.
19 S. Martwiset, R. C. Woudenberg, S. Granados-Focil, O. Yavuzcetin, M. T. Tuominen and E. B. Coughlin, *Solid State Ionics*, 2007, **178**, 1398–1403.
20 C. Versek and M. T. Tuominen, unpublished results.
21 J. Catalan, J. L. M. Abboud and J. Elguero, *Adv. Heterocycl. Chem.*, 1987, **41**, 187–274.
22 J. Catalan, R. M. Claramunt, J. Elguero, J. Laynez, M. Menendez, F. Anvia, J. H. Quian, M. Taagepera and R. W. Taft, *J. Am. Chem. Soc.*, 1988, **110**, 4105–4111.
23 T. Cardinaels, J. Ramaekers, P. Nockemann, K. Driesen, K. Van Hecke, L. Van Meervelt, S. Lei, S. De Feyter, D. Guillon, B. Donnio and K. Binnemans, *Chem. Mater.*, 2008, **20**, 1278–1291.
24 M. B. Goldfinger and T. M. Swager, *J. Am. Chem. Soc.*, 1994, **116**, 7895–7896.
25 J. C. Loren, A. Krasinski, V. V. Fokin and K. B. Sharpless, *Synlett*, 2005, 2847–2850.
26 K. Goossens, S. Wellens, K. Van Hecke, L. Van Meervelt, T. Cardinaels and K. Binnemans, *Chem.–Eur. J.*, 2011, **17**, 4291–4306.
27 H. Fujioka, K. Murai, Y. Ohba, A. Hiramatsu and Y. Kita, *Tetrahedron Lett.*, 2005, **46**, 2197–2199.
28 K. Omura and D. Swern, *Tetrahedron*, 1978, **34**, 1651–1660.
29 K. Sonogashira, *J. Organomet. Chem.*, 2002, **653**, 46–49.
30 R. Huisgen, *Proc. Chem. Soc., London*, 1961, 357.
31 H. C. Kolb, M. G. Finn and K. B. Sharpless, *Angew. Chem., Int. Ed.*, 2001, **40**, 2004–2021.
32 Z. Zhou, R. Liu, J. H. Wang, S. W. Li, M. L. Liu and J. L. Bredas, *J. Phys. Chem. A*, 2006, **110**, 2322–2324.
33 C. Nagamani, C. Versek, M. Thorn, M. T. Tuominen and S. Thayumanavan, *J. Polym. Sci., Part A: Polym. Chem.*, 2010, **48**, 1851–1858.
34 M. J. Frisch, G. W. Trucks, H. B. Schlegel, G. E. Scuseria, M. A. Robb, J. R. Cheeseman, G. Scalmani, V. Barone, B. Mennucci, G. A. Petersson, H. Nakatsuji, M. Caricato, X. Li, H. P. Hratchian, A. F. Izmaylov, J. Bloino, G. Zheng, J. L. Sonnenberg, M. Hada, M. Ehara, K. Toyota, R. Fukuda, J. Hasegawa, M. Ishida, T. Nakajima, Y. Honda, O. Kitao, H. Nakai, T. Vreven, J. A. Montgomery, Jr, J. E. Peralta, F. Ogliaro, M. Bearpark, J. J. Heyd, E. Brothers, K. N. Kudin, V. N. Staroverov, R. Kobayashi, J. Normand, K. Raghavachari, A. Rendell, J. C. Burant, S. S. Iyengar, J. Tomasi, M. Cossi, N. Rega, J. M. Millam, M. Klene, J. E. Knox, J. B. Cross, V. Bakken, C. Adamo, J. Jaramillo, R. Gomperts, R. E. Stratmann, O. Yazyev, A. J. Austin, R. Cammi, C. Pomelli, J. W. Ochterski, R. L. Martin, K. Morokuma, V. G. Zakrzewski, G. A. Voth, P. Salvador, J. J. Dannenberg, S. Dapprich, A. D. Daniels, Ö. Farkas, J. B. Foresman, J. V. Ortiz, J. Cioslowski, and D. J. Fox, *Gaussian 09*, Gaussian, Inc., Wallingford CT, 2009.